International Journal of Biological Macromolecules 163 (2020) 718–729

Contents lists available at ScienceDirect

International Journal of Biological Macromolecules

journal homepage: http://www.elsevier.com/locate/ijbiomac

# It takes two to tango - The case of thebaine 6-*O*-demethylase

Sangita Kachhap [a,1], Zuzanna Wojdyla [a,1], Paulina Komorek [a], Anna Kluza [a], Katarzyna Kurpiewska [a,b], Barbara Jachimska [a], Tomasz Borowski [a,*]

[a] Jerzy Haber Institute of Catalysis and Surface Chemistry, Polish Academy of Sciences, Niezapominajek 8, PL-30239 Krakow, Poland
[b] Department of Crystal Chemistry and Crystal Physics, Faculty of Chemistry, Jagiellonian University, Gronostajowa 2, PL-30387 Krakow, Poland

ARTICLE INFO

*Article history:*
Received 1 April 2020
Received in revised form 26 June 2020
Accepted 2 July 2020
Available online 7 July 2020

*Keywords:*
*O*-demethylase
2-oxoglutarate dependent oxygenase
Thebaine
Morphine
Non-heme iron
Reaction mechanism

ABSTRACT

Thebaine 6-*O*-demethylase (T6ODM) is an Fe(II)/2-oxoglutarate-dependent dioxygenase catalysing two oxidative *O*-demethylation reactions in morphine biosynthesis. Its crystal structure revealed a large active site pocket which is at least two times larger than necessary to accommodate a substrate (thebaine or oripavine) molecule. Since so far no crystal structures have been obtained for enzyme-substrate complex, which is necessary to explain the enzyme regiospecificity towards the C6-bound methoxy group, in this work we used computational methods and multi-parametric surface plasmon resonance measurements to elucidate the most likely structure of this complex and the reaction mechanism starting therefrom. Results of simulations and experiments unanimously indicate that the enzyme-substrate complex of T6ODM has a 1:2 stoichiometry. The key residues responsible for substrate binding are: Val-128, Glu-133, Met-150 and Agr-219 for the substrate in the distal position, and Asp-144, Leu-235 and Leu-353 for the proximal substrate molecule. QM/MM and DFT calculations show that the oxo ligand is bound trans to His-295 and the enzyme catalyzes hydroxylation of the C6-bound methoxy group according to the established rebound mechanism. The final stage of the demethylation reaction, which includes deformylation and enol-keton tautomerization steps, is most likely catalysed by water molecules and takes place in the solvent.



## 1. Introduction

The plant enzymes from the non-heme Fe(II)/2-oxoglutarate-dependent dioxygenase (ODD) superfamily catalyze diverse reactions including desaturation, hydroxylation, and demethylation [1]. T6ODM, a dioxygenase from *Papaver somniferum* (opium poppy), is a member of the ODD superfamily. It catalyzes the regiospecific 6-*O*-demethylation of morphine precursors thebaine and oripavine in the morphine biosynthesis pathway [2]. A closely related codeine *O*-demethylase (CODM) also participates in this process and catalyzes the 3-*O*-demethylation of thebaine and codeine (Fig. 1) [3]. These two proteins, both belonging to ODD family, share 72.8% of amino acid sequence identity.

The X-ray crystal structures of T6ODM with bound succinate (SIN) (PDB: 5O7Y) and 2-oxoglutarate (2OG) (PDB: 5O9W) have already been published [4]. Through structural comparison to other members of the same family it was noted that both T6ODM and anthocyanidin synthase (ANS), which has 32.1% sequence identity with T6ODM, have similarly spacious active sites (1005 Å$^3$ and 769 Å$^3$ for T6ODM and ANS, respectively). The crystal structure of ANS revealed that the protein binds two molecules of dihydroquercetin and a buffer molecule in the binding pocket [5,6]. Notably, the substrates for T6ODM and ANS are of comparable volume (within the range of 240–290 Å$^3$) [4], which suggests that it would be feasible for T6ODM to accommodate two molecules of the substrate in the binding pocket, as ANS does.

In this study we have determined the number of substrate molecules binding to the enzyme active site. The 1:1 and 1:2 T6ODM-substrate complexes were generated through molecular docking. Further, molecular dynamics (MD) simulation of these complexes shows that in the 1:1 complex, the substrate is not inclined to remain close to the metal cofactor and it diffuses through the binding pocket to a distal binding site. In contrast, the 1:2 complex, in which one substrate molecule docked proximally to the metal center and another at the distal site, is stable during MD simulation. Thus, combined docking and MD simulations studies suggest there is a preference for binding two molecules of the substrate to the active site. The same conclusion is further supported by the results of surface plasmon resonance measurements

* Corresponding author.
*E-mail address:* ncborows@cyf-kr.edu.pl (T. Borowski).
[1]These authors contributed equally.

https://doi.org/10.1016/j.ijbiomac.2020.07.030
0141-8130/

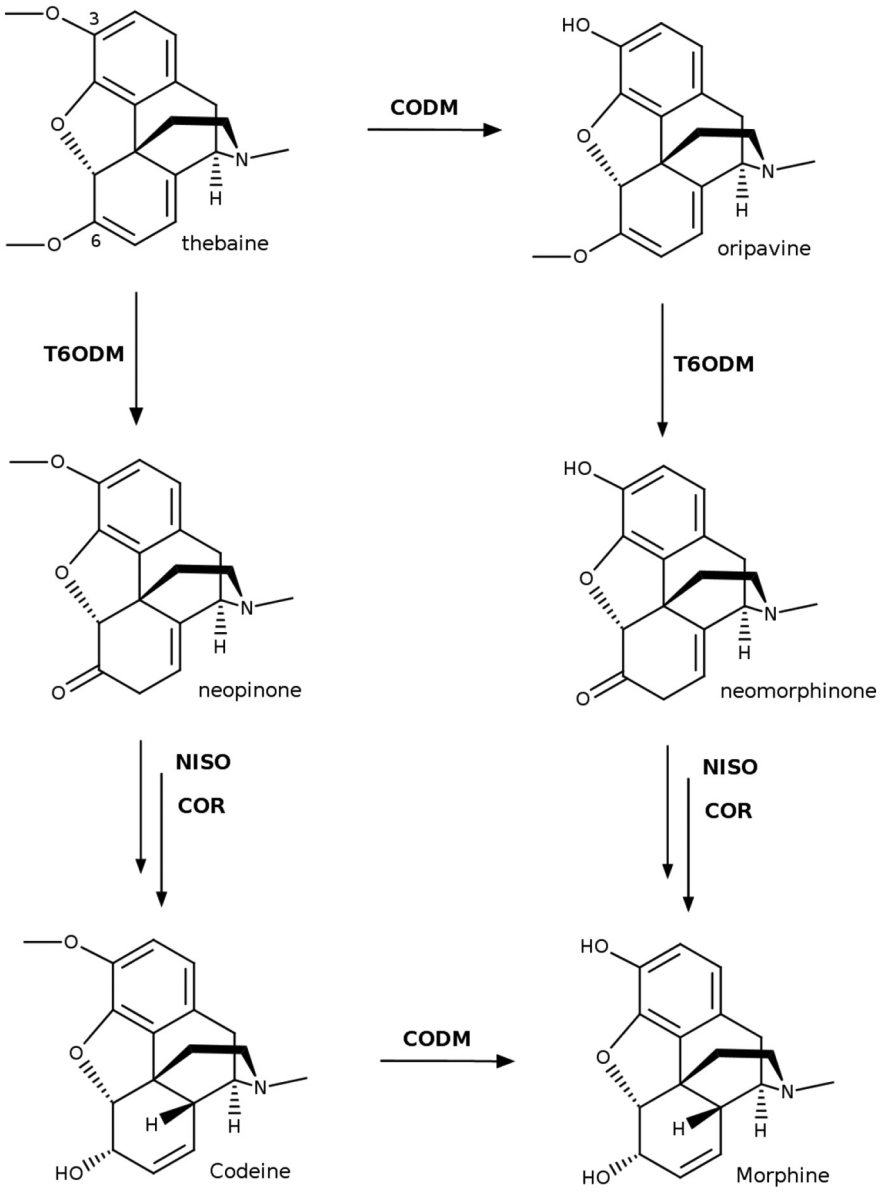


**Fig. 1.** Final stages of morphine biosynthesis. NISO - neopinone isomerase, COR - codeinone reductase [43].

(SPR). Since the detailed mechanism of thebaine and oripavine 6-*O*-demethylation by T6ODM is still unknown, we further extended this study by exploring the reaction mechanism with QM/MM and QM methods.

## 2. Materials and methods

### *2.1. Model set up for docking and MD simulations*

The structure of charge-neutral thebaine was downloaded from the Cambridge Structural Database (TICTUU) [7]. Oripavine was constructed on the basis of thebaine by substituting the C3-bound methoxy group with a hydroxy one. Both ligands were protonated at the tertiary nitrogen atom as $pK_a$ for thebaine and oripavine equals to 8.2 and 8.4, respectively [8]. The structures of the ligands were optimized at the B3LYP-D3/6-311G(d,p) level [9,10]. Electrostatic potential (ESP) for the optimized geometries was calculated at the HF/6-31G* level, which is consistent with the general AMBER force field (GAFF) [11], and atomic charges of the molecules were later obtained within the restrained electrostatic potential (RESP) formalism [12]. The remaining force field parameters of the ligands were taken from GAFF.

The model of the protein was prepared on the basis of the crystal structure for T6ODM:SIN (PDB: 5O7Y). Succinate was replaced with 2OG after superposition on the PDB structure 1GP5. Oxygen atoms from ethylene glycol coordinated by metal in the active centre were replaced by waters, and the Ni(II) ion was replaced with Fe(II). Subsequent comparison with the T6ODM:2OG structure (PDB: 5O9W) showed that there were no significant differences in the 2OG binding mode in this model and the actual T6ODM:2OG crystal structure, which was solved afterwards. Hydrogen atoms were added to the protein and crystallographic waters with the LEaP program from the AmberTools 14 package [13], which was followed by a visual inspection. The model was solvated by creating a box of TIP3P water around the protein [14]. Distance between the wall of the box and the closest atom of the protein was equal to 10 Å. The system was neutralised by adding 17 $Na^+$ ions. Protein residues, except those directly coordinated to the Fe(II) ion, were described with the AMBER ff03 force field [15], whereas the missing bonded parameters for the metal cofactor were calculated with the use of a model of the active site optimized at the

B3LYP/lanl2dz level [16]. The model consists of Fe(II) ligated by His-238, His-295, Asp-240 side chains, a water molecule and 2OG. Atomic charges were calculated using RESP based on ESP calculated with Gaussian 09 at the B3LYP/cc-pVTZ/IEFPCM ($\varepsilon = 4$, $r = 1.4$ Å) level [17].

### 2.2. Protein-ligand docking

Docking of substrates to T6ODM was performed with AutoDock 4 [18]. Amber ff03 atomic charges and atomic charges obtained with the RESP procedure were used for protein and ligand molecules, respectively. The search space was described by a grid with spacing equal to 0.375A and a size of 40 Å, 50 Å, 45 Å in the *x*-, *y*-, and *z*-axis, respectively. In each search a population of 100 conformations was generated by a Lamarckian Genetic Algorithm and then analysed by clustering with cluster cut-off determined by rmsd equal to 1.5 Å. The most promising enzyme-substrate complexes were chosen on the basis of both the lowest energy and the population of the cluster.

### 2.3. MD simulations

Systems were prepared for the molecular dynamics simulation in the following way. First, the solvent molecules were relaxed in a minimisation, during which all coordinates of the solute atoms were restrained with a 500 kcal/mol harmonic potential. The coordinates of the Fe(II) ion and its first coordination shell were restrained using 500 kcal/mol harmonic potential through all steps of minimisation as well as through the MD simulation, to retain its correct geometry. In the following minimisation step the restraining potential for the protein was reduced to 10 kcal/mol and for the final minimisation step the restraining potential was removed. After minimisation, the system was heated from 0 to 300 K in 100 ps and equilibrated for the next 1 ns. These steps, unless stated otherwise, were followed by MD production run at a constant temperature equal to 300 K and a constant pressure equal to 1 atm. The length of the simulations varied from 30 ns (for screening simulations) to 80 ns (for the final ones). Stable parts of the trajectory i.e. 50 ns long, were selected for further analysis. Time step for the simulations was equal to 2 fs and consequently, SHAKE algorithm was employed to constrain all bonds involving hydrogen atoms [19,20]. Simulations were performed under periodic boundary conditions and the particle-mesh Ewald method was used for calculation of electrostatic energy of a cell [21]. Trajectory files were later analysed with the use of the cpptraj code from the AMBER14 package [22].

### 2.4. QM/MM calculations

Cluster representative structures from MD trajectories were taken for further calculations. Gaussian 16 was employed for ONIOM (QM/MM) [23]; MM charges and force field parameters for the metal cofactor were taken from the MD set-up. First, the T6ODM:2OG:thebaine and T6ODM:2OG:oripavine cluster representative structures from MD trajectories were optimized. Then, from the respective optimized structures, T6ODM:SIN:thebaine and T6ODM:SIN:oripavine complexes were generated. The system considered for calculations consisted of protein, Fe(II)/Fe(IV)=O, substrate (thebaine/oripavine), co-substrate/its decarboxylation product (2OG/SIN), and water molecules up to 20 Å from Fe. The QM region in T6ODM:2OG:thebaine and T6ODM:2OG:oripavine comprised of Fe, side chains of active site residues His-238, Asp-240, His-295, two molecules of water, and 2OG truncated up to C4. For the T6ODM:SIN:thebaine and T6ODM:SIN:oripavine models, the QM parts consist of the ferryl group (Fe-oxo), the side chains of active site residues His-238, Asp-240, His-295, proximal thebaine or oripavine and succinate truncated up to C3. Protein residues, dystal substrate and water molecules up to 15 Å from Fe were relaxed during geometry optimization, while the rest was frozen. Two-layer ONIOM scheme was used for all QM/MM calculations [24]. The UB3LYP functional and the def2-SVP basis set were employed for geometry optimization [25]. Electrostatic interaction between the QM and MM regions was treated by mechanical embedding in which these interactions are calculated at the MM level. After geometry optimization, new updated charges for the QM part were calculated for each reaction species. To this end, electrostatic potential (ESP) around the QM region was calculated with the presence of atomic charges from the MM part, which polarize the QM electron density. Charges of MM atoms located one and two bonds away from the QM region were not included, consistently with the default electronic embedding scheme in Gaussian. Final energy values presented here combine single point ONIOM(UB3LYP-D3:Amber) energy calculated with the def2-TZVP basis set [25], electronic embedding and thermal correction to Gibbs free energy. Thermal correction was calculated at the same level as geometry optimization, i.e. ONIOM with mechanical embedding and the def2-SVP basis set.

### 2.5. DFT calculations

Hemiacetal derivatives generated from thebaine and oripavine in the T6ODM active site were further considered for calculating reaction energy profiles of their transformation to neopinone and neomorphinone, respectively. This process will take place in two steps, first hemiacetal derivatives will decompose to enol derivatives with the release of formaldehyde, then, in the second step, enolic intermediates will tautomerize to ketone products: neopinone and neomorphinone, respectively. During the deformylation step one water molecule was included in the model as a mediator in proton transfer. The models considered for enol to ketone tautomerization included, for sterical reasons (vide infra), two water molecules.

A hybrid density functional B3LYP [9] combined with Grimme's dispersion correction D3 with the Becke-Johnson damping scheme [10] was employed. The geometry of all reaction stationary points was optimized by applying split valence polarized basis set def2-SVP [25], self-consistent reaction field (SCRF) method with CPCM (conductor like polarizable continuum model) [26] and the probe radius set to 1.4 Å. Vibrational normal modes and their frequencies were calculated at the same level and further used to compute zero-point energy (ZPE) corrections to the electronic energy. Triple zeta valence polarized basis set def2-TZVP [25] along with the D3 dispersion correction and SCRF method was used for calculating more accurate single-point energies of all the reaction species. These energy values, combined with ZPE corrections, are presented and discussed here. All calculations were done with Gaussian 16 [23].

### 2.6. Multi-Parametric Surface Plasmon Resonance (MP-SPR)

T6ODM was expressed and purified, as described previously [4]. Interactions between molecules of T6ODM and thebaine were followed by using the Multi-Parametric Surface Plasmon Resonance (MP-SPR) model Navi 200 (BioNavis Ltd., Finland). MP-SPR is a real-time label-free method [27–30], which consists of a goniometer and a prism coupling-based device (Krechmer mode) and two independent flow channels with two lasers with different wavelengths 670 nm (FC1) nm and 785 nm (FC2). The system is also equipped with an integrated peristaltic pump. The MP-SPR apparatus worked in a wide angular scan range (40–78°). Effectiveness of interactions between molecules can be determined by monitoring changes in resonance angle and calculating the changes into the adsorbed mass of individual reagents according to the equation:

$$\Delta\Gamma_{MP-SPR} = \frac{\Delta\Theta_{MP-SPR} k d}{\frac{dn}{dc}} \quad (1)$$

where $\Delta\Theta_{MP-SPR}$ is the change of the MP-SPR angle, $\frac{dn}{dc}$ is the refractive index increment and $\frac{dn}{dc} \approx 0.166$ cm$^3$/g; $k$ is an instrument constant, $d$ is

the thickness of the adsorbed layer, $k \times d \approx 10 \times 10^{-7}$ nm/deg. for $\lambda = 670$ nm (FC1) while for 785 nm (FC2) - $k \times d \approx 1.9 \times 10^{-7}$ nm/deg. All experiments were performed at a constant flow rate of 50 μL/min. MP-SPR sensors with a glass slide base of 50 nm of gold were produced by BioNavis. Specific reagents were sequentially introduced into the system for a specified length of time. The mass of each adsorbed reagent was calculated separately, and then the ratio of the masses of interacting molecules was calculated. It can be directly converted to the stoichiometric ratio of interacting substances using their molar masses.

## 3. Results and discussion

### 3.1. Simulations of T6ODM - substrate complexes

The structure of the enzyme-substrate complex is key to understanding the origins of substrate and reaction specificities at the atomic level. With the available X-ray structure of T6ODM we did in silico docking and molecular dynamics simulations for T6ODM:2OG:thebaine/oripavine complexes with the aim of obtaining structural models that would provide us a glimpse into the enzyme-substrate interactions. Interestingly, the simulation results suggest that T6ODM requires two molecules of a substrate, i.e. thebaine or oripavine, to form a complex that facilitates substrate demethylation (Fig. 2).

The first molecule of the substrate (thebaine-1, shown as blue sticks in Fig. 2) is bound in a position distant from the iron cofactor and its presence is crucial for the subsequent binding of the second molecule of substrate, which binds in the immediate proximity of iron, i.e. in the catalytic position, shown as cyan sticks (thebaine-2).

#### 3.1.1. Complexes with one molecule of substrate

For the great majority of enzymes, the enzyme-substrate complex has a 1:1 enzyme:substrate stoichiometric ratio and, as a consequence, it was natural to consider such a complex also for T6ODM. MD simulations (in total 15 'screening' simulations, each started from a different initial geometry generated via docking) of docked complexes show that a substrate molecule departs from the metal center and moves relatively freely in the binding pocket. Importantly, this migration starts during the initial stage of the simulation, i.e. within the first 10 ns. In nine out of 15 simulations, the single substrate molecule migrated towards the vicinity of a potential distal binding site covering a distance of approximately 10 Å within ca. 10–20 ns. Once relocated, the substrate remained at this site in all simulations, which suggests that this region can effectively bind the substrate and is the preferred locus for substrate binding in the 1:1 *E*-S complex. This assumption was further verified with 70 ns long MD simulations for T6ODM:2OG:thebaine and T6ODM:2OG:oripavine complexes (for details of the MD protocol, consult Fig. S1).

The distal site hosts hydrophobic residues Val-128 from the α6/β3 and Gly-132 from the β3/β4 loop regions, Ile-148 and Met-150 from the β4 strand, which interact with the benzylisoquinoline core of the substrate (Fig. 3A, thebaine-1 shown as blue sticks, Fig. 3C, oripavine-1 shown as dark blue sticks). Native contact analysis of the stable part of the final MD trajectory indicates that the interaction of Val-128 with the inner (concave) face of the core of the substrate is most frequent (Fig. 3B and D). The amino acid sequence of the β4 strand is different in T6ODM and CODM, which suggests that this region might be responsible for the substrate specificity of T6ODM.

Contacts between a protein and morphinian compounds are based on hydrophobic interactions, as demonstrated by the crystal structure of the G-protein-coupled μ-opioid receptor (μ-OR) complexed with β-funaltrexamine (PDB: 4DKL). The benzylisoquinoline moiety of the irreversible morphinan antagonist forms hydrophobic contacts with adjacent valine, methionine and isoleucine side chains [31]. Notably, in this structure, the orientation of the valine side chain with respect to the opioid moiety of the antagonist is analogous to that obtained for Val-128 and the substrate in T6ODM:2OG:thebaine and T6ODM:2OG:oripavine complexes. Similar binding modes were also obtained by a QM/MM method for a complex of cytochrome P450 2D6 with dextromethorphan, whose core bears strong resemblance to the core of thebaine, only lacking the C3-bound methoxy group and the O atom of the 5-membered heterocyclic ring [32]. In this case, the orientation

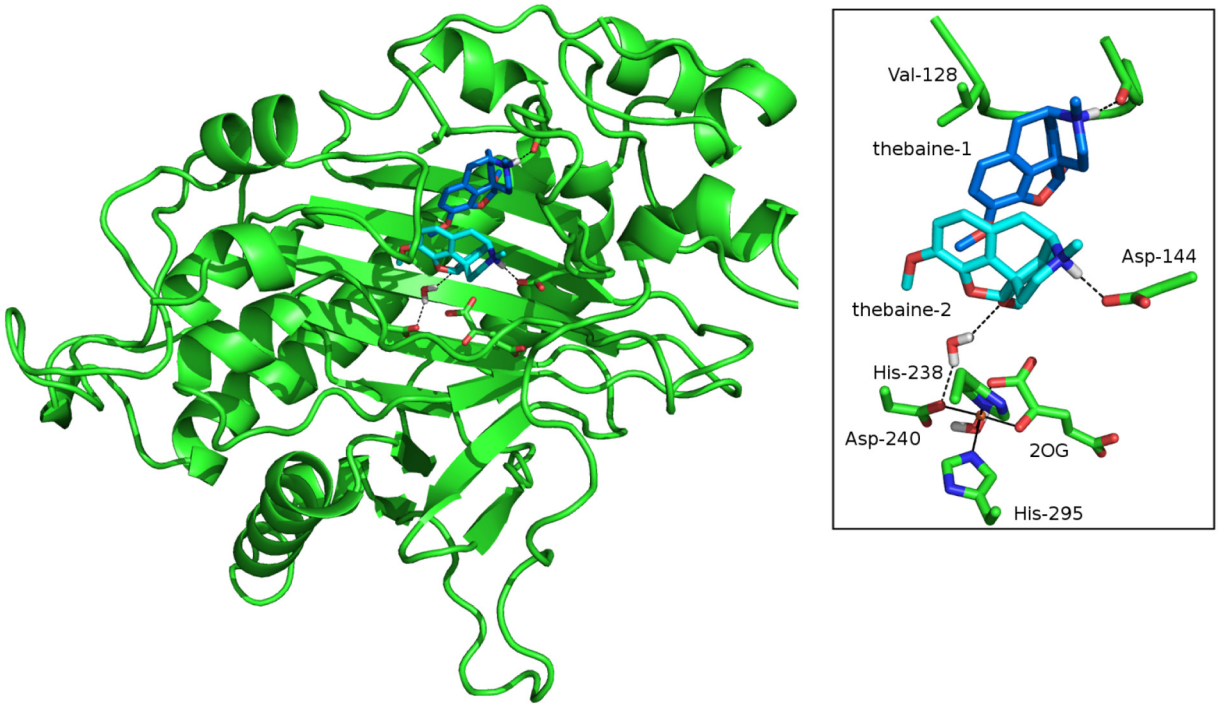


**Fig. 2.** Structure of a model for T6ODM:2OG:$(thebaine)_2$ complex. Thebaine (blue - distant position and cyan - proximal position) and side chains of residues involved in hydrogen bonding with the substrate are shown as sticks. Figure rendered using PyMOL.

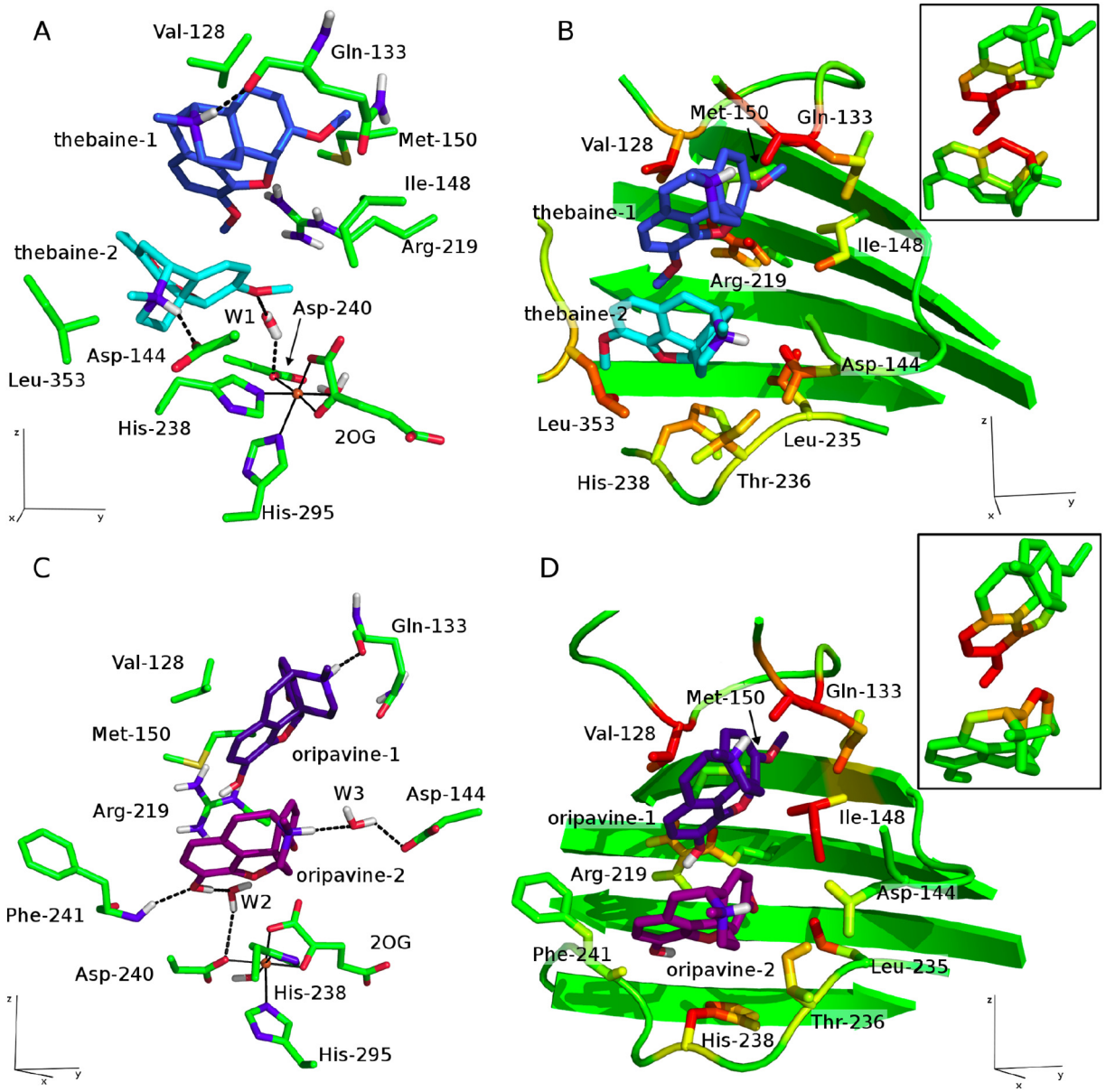


**Fig. 3.** Detailed view of the binding pocket. (A) Thebaine (the molecule bound in the distal site - blue, the one in the catalytic position - cyan) bound to T6ODM:2OG, (B) T6ODM:2OG:(thebaine)$_2$ complex with amino acids colored according to the strength of native contacts with thebaine on scale from green (no contacts) to red (frequent contacts). Colour of thebaine in the inset reflects strength of contacts between the two molecules of the substrate. (C) Oripavine (the molecule bound in the distal site - dark blue, the one in the catalytic position - purple) bound to T6ODM:2OG, (D) T6ODM:2OG:(oripavine)$_2$ complex with the binding pocket colored as in B.

of the substrate within the active site is governed by interactions between the core of the molecule and hydrophobic moieties of Ser, Ala, Val, and Thr.

Apart from hydrophobic effects, the 1:1 T6ODM:substrate is stabilized by several hydrogen bonds. Thebaine and oripavine interact with the protein in a very similar way, i.e. the tertiary amine group of the substrate forms a hydrogen bond with the Gln-133 main chain carbonyl group. Arg-219, which is initially engaged in electrostatic interactions with 2OG, changes its conformation and forms a weak hydrogen bond with the C3-bound methoxy (or hydroxy) group of the substrate.

For substrates bound in the distal binding site, distances between the methoxy groups and the iron cofactor are on the order of 10 Å, which is clearly too far apart for a direct reaction. On the other hand, it has been previously observed that ANS, a closely related enzyme from the ODD family, binds two molecules of its substrate in the vicinity of the active site (PDB: 1GP5) [5]. Therefore, we considered the possibility that once the first substrate molecule is bound in the distal site, the second molecule will bind in the proximal position.

### *3.1.2. Complexes with two molecules of substrate*

Combined docking and MD simulations for 1:2 E:S complexes, showed the possibility that in the presence of one substrate molecule bound in the distal site another substrate molecule can bind in the vicinity of the iron cofactor. Docking the second molecule of oripavine to the 1:1 T6ODM:substrate complex resulted in two poses, both of which presented the C6-bound methoxy group to the iron binding site. The structures were grouped into two clusters that were distant from each other in energy by 0.5 kcal/mol (Fig. S2). The orientation promoting demethylation at the C3 position was not obtained presumably due to either unfavourable steric interaction between the core of the substrate and the side chains of residues in the second coordination sphere of the iron cofactor or electrostatic interaction between the arginine-219

residue and tertiary amino group of the substrate. The docking was followed by MD simulations that yielded stable structures for the 1:2 E:S complexes. Notably, in the resulting structures, the orientation of the second substrate molecule with respect to the iron cofactor will promote demethylation at the C6-bound methoxy group (Fig. 3A and C).

This substrate molecule is bound in a hydrophobic pocket formed by Leu-235, aliphatic chain of His-238, Ile-148, ring A and the C3-bound methoxy group of the substrate molecule bound in the distal site; the latter forms close contacts with the inner face of the substrate molecule proximal to the iron cofactor (Fig. 3B and D). Hence, the substrate molecule bound in the distal site participates in the binding of the substrate in the immediate vicinity of the iron cofactor.

The substrate in the proximal position of the 1:2 T6ODM:substrate complex is stabilized by the interaction between the charged amino group of thebaine/oripavine and the carboxyl group of Asp-144. It is worth noting that very similar interactions are necessary for the formation of a complex between P450 2D6 and dextromethorphan, as inferred from kinetic studies for this system [33]. The C6-bound methoxy group of thebaine-2 forms a water-bridged hydrogen bond with the carboxyl group of Asp-240 (Fig. 3A). A formation of hydrogen bonds is accompanied by hydrophobic interactions with Leu-353 and the C3-bound methoxy group of the substrate bound in the distal position (Fig. 3A).

The mutual arrangement of the substrate-2 and the metal cofactor is appropriate for the subsequent reaction, i.e. the distance between the carbon atom of the C6-bound methoxy group of substrate-2 and O1 of 2OG, which is an estimate of the substrate-oxo ligand distance, is 4.1 ± 0.5 Å (mean and standard deviation computed for a sample of $N = 7600$ MD snapshots) for thebaine-2 (shown as cyan sticks in Fig. 3A) and 3.9 ± 0.5 Å for oripavine-2 (sample of $N = 5561$, shown as purple sticks in Fig. 3C).

### 3.2. Stoichiometry of T6ODM:Thebaine interaction probed by MP-SPR

The effectiveness of complex formation between T6ODM and thebaine was probed using the MP-SPR method. The experiments were carried out in a buffer solution containing 50 mM TRIS, 150 mM NaCl, pH = 7.4 (TRIS-NaCl). The MP-SPR method uses a sensor covered with a layer of gold, which has an isoelectric point at pH = 3.4. At pH 7.4 the sensor has a negative charge, the value of the zeta potential of the surface is $\zeta = -30$ mV [34]. Under the same conditions, T6ODM has a negative charge manifesting in $\zeta = -17$ mV, an isoelectric point of T6ODM is located at pH 5.1. In order to form a stable T6ODM layer on the sensor surface, the latter has been properly functionalized using a biocompatible polyelectrolyte, in this case, poly-L-lysine (PLL). PLL at pH = 7.4 and ionic strength $I = 1 \times 10^{-2}$M has a positive charge manifesting in $\zeta = +38$ mV. PLL characterized by molecular weight in the range of Mw = 40,000–70,000 D at a concentration of 50 ppm was used for surface functionalization. PLL was adsorbed for 30 min on the sensor surface to obtain a stable polyelectrolyte layer, after which the system was rinsed with TRIS-NaCl solution for 30 min. PLL molecules adsorb irreversibly on the sensor surface and thus form a surface suitable for T6ODM immobilization. T6ODM at a concentration of 15 or 30 ppm was adsorbed for 60 min until a saturated layer was obtained, and then the system was rinsed for 60 min with TRIS-NaCl solution. Next, the co-substrate analog, N-oxalylglycine (NOG), in stoichiometric excess, was adsorbed onto the formed T6ODM layer for 30 min, and then the system was rinsed with a solution of TRIS-NaCl for 30 min. In the last stage, thebaine at a concentration of 5 ppm was introduced into the system for 45 min until reaching the saturation level. The lack of desorption when rinsing the system with TRIS-NaCl solution confirmed that the obtained layer is irreversibly adsorbed on the sensor surface. Resonance angle measurements were carried out for two laser wavelengths: 670 nm (channel - FC1) and 785 nm (channel - FC2). On this basis, using Eq. (1), the mass values of each layer adsorbed on the sensor surface were calculated. The obtained changes in the resonance angle during the experiment in the MP-SPR method were converted into adsorbate mass per area, which are presented in Fig. 4, whereas the values of the adsorbed mass of individual layers are presented in Table 1.

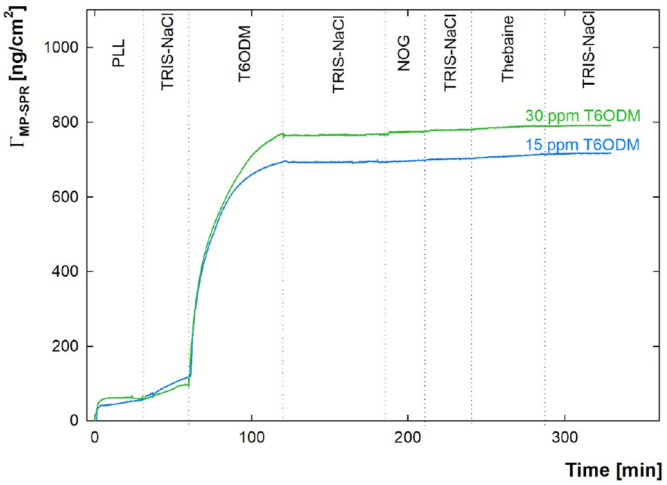


**Fig. 4.** T6ODM:thebaine complex formation determined using the MP-SPR method using channel FC2 (795 nm). The isotherm for T6ODM adsorbed from the 15 ppm solution is presented in blue, whereas in green the isotherm for adsorption from the 30 ppm T6ODM solution.

The molar ratio of interacting thebaine and T6ODM ($n_{thebaine}$) / $n_{T6ODM}$) molecules in the presence of N-oxalylglycine was determined based on the adsorbed mass using the following equation:

$$\frac{n_{thebaine}}{n_{T6ODM}} = \frac{\Delta\Gamma_{MP-SPR}^{thebaine} * M_{T6ODM}}{\Delta\Gamma_{MP-SPR}^{T6ODM} * M_{thebaine}} \quad (2)$$

where $\Delta\Gamma_{MP-SPR}^{T6ODM}$ - T6ODM adsorbed mass, $\Delta\Gamma_{MP-SPR}^{thebaine}$ – thebaine adsorbed mass, $M_{thebaine}$ – the molar mass of thebaine, $M_{T6ODM}$ – the molar mass of T6ODM. According to our calculations, the adsorbed mass of T6ODM equals to 577.048 and 671.022 ng/cm$^2$ for the experiments with T6ODM concentration of 15 and 30 ppm, whereas the mass of thebaine adsorbed on the formed layers, from a solution of 5 ppm concentration, is 9.578 and 10.690 ng/cm$^2$, respectively. The molar ratio of thebaine associated with T6ODM is two independently of the concentration of adsorbed T6ODM and the channel used. The steady level of the last two stages of the measurements, representing adsorption of thebaine and introducing TRIS-NaCl, indicates that the molecules of thebaine are bound irreversibly even after rinsing the system with solvent, which shows that formed complexes are stable. These findings, based on experimental results of the ratio of masses of adsorbed reagents, corroborate the conclusions about the 1:2 stoichiometry of T6ODM:substrate complexes formulated based on the results of docking and MD simulations (presented above).

### 3.3. QM/MM structures of T6ODM:SIN:Substrate (thebaine/oripavine) complexes

The complexes of T6ODM:SIN:thebaine and T6ODM:SIN:oripavine, generated from the MD simulated T6ODM:2OG:thebaine and T6ODM:2OG:oripavine complexes by truncation of 2OG to form SIN, has 87.8 and 89.9° narrow His-295(NE2)-Fe-oxo angle, respectively, which means the oxo ligand is positioned trans to His-238. One more complex was generated from each of the complexes with wider His-295(NE2)-Fe-oxo angle i.e. 174.7 and 174.6°, respectively, where the oxo ligand is positioned trans to His-295. In the final QM/MM optimized structures, the His-295(NE2)-Fe-oxo angles were noted to be 96.7, and 174.8° for the thebaine complex, 101.7, and 171.5° for oripavine. The

**Table 1**
MP-SPR results of T6ODM-thebaine complex formation obtained for T6ODM in a concentration of 15 and 30 ppm. Parameters: $\Gamma_{T6ODM}/\Gamma_{thebaine}$ – the ratio of the adsorbed mass of T6ODM to adsorbed mass of thebaine, $n_{thebaine}/n_{T6ODM}$ – the molar ratio of thebaine molecules to T6ODM molecules.

| channel | concentration of T6ODM [ppm] | mass of adsorbed T6ODM [ng/cm$^2$] | mass of adsorbed thebaine [ng/cm$^2$] | $\Gamma_{T6ODM}/\Gamma_{thebaine}$ | $n_{thebaine}/n_{T6ODM}$ |
|---|---|---|---|---|---|
| FC1 (670 nm) | 15 | 552.148 | 8.823 | 62.58 | 1.99 |
| FC2 (795 nm) | 15 | 577.048 | 9.578 | 60.25 | 2.18 |
| FC1 (670 nm) | 30 | 602.120 | 9.477 | 63.53 | 2.07 |
| FC2 (795 nm) | 30 | 671.022 | 10.690 | 62.78 | 2.09 |

wide angle complexes (thebaine −7.3 kcal/mol and oripavine −9.0 kcal/mol) are comparatively more stable than the narrow angle counterparts and are also characterized by a close distance between the oxo ligand and the C-6 bound methoxy group of thebaine or oripavine, so they were considered for further calculations.

MD simulations of both the complexes were performed and followed by clustering analysis. Then, cluster representative structures were taken for further calculation of reaction energy profiles. In both the QM/MM optimized enzyme-substrate complexes, five ligands: His-238, Asp-240, His-295, SIN and oxo are coordinated to Fe(IV). The Fe(IV)-oxo bond length is 1.6 Å, whereas other ligands are at distances of approximately 1.9 to 2.0 Å. In the thebaine complex, there are five water molecules within the 5 Å distance range of Fe. These water molecules make hydrogen bond networks with Phe-241, Arg-19, Asp-210, Asn-221, SIN, and thebaine; the structures of these networks are in good agreement with the MD simulation cluster representative structure. In the oripavine complex, two water molecules are present within the 6 Å distance range of Fe. These water molecules are involved in hydrogen bonding with other water molecules and the oxo ligand, and the same was observed in the MD simulation cluster representative structure.

### 3.4. Computational investigations into reaction mechanism

The general mechanism of Fe(II)/2-oxoglutarate-dependent dioxygenases begins with the binding of 2-oxoglutarate and the specific substrate to the enzyme active site. Then, molecular oxygen binds and elicits oxidation of 2-oxoglutarate into succinate with the release of $CO_2$ and formation of reactive Fe(IV)-oxo intermediate, which subsequently oxidises the substrate [1,36]. Starting from the 1:2 complex, containing reactive Fe(IV)-oxo intermediate and succinate, employing QM/MM we calculated the energy profile for hydrogen abstraction by Fe(IV)-oxo from the substrate (thebaine/oripavine) and then for OH rebound to the alkyl radical. Further, using DFT calculations we also explored the mechanism of transformation of thebaine and oripavine derived hemiacetals (formed after OH rebound) to neopinone and neomorphinone, respectively.

#### 3.4.1. T6ODM-catalysed hydroxylation

In order to understand the C6 bound oxygen demethylation of thebaine and oripavine to neopinone and neomorphinone, respectively, first, we investigated the mechanism of hydrogen abstraction by ferryl (Fe(IV)-oxo) intermediate from the methyl group connected with C6 bound oxygen of both substrates. Then we calculated the energy barrier associated with OH (formed after H abstraction) rebound to radical reaction intermediate and formation of hemiacetal as a product. During the demethylation of both substrates, it was observed that Fe(IV) is reduced to Fe(III) after hydrogen abstraction and after the OH rebound step Fe(III) is further reduced to Fe(II); the spin populations of Fe throughout the reaction are given in Table 2.

*3.4.1.1. T6ODM:SIN:thebaine.* For all the optimized reaction species, we calculated single point energy with mechanical embedding followed by electronic embedding single point calculation to incorporate polarization of the QM wave function due to presence of the MM environment. The calculated free energy barrier (t-TS1) for hydrogen abstraction from thebaine is 20.1 kcal/mol (Fig. 5), and in the transition state t-TS1 the distance between the oxo ligand and hydrogen to be extracted is 1.12 Å (Fig. 6B). This barrier is a bit high, but a high barrier for H-atom abstraction by another ODD enzyme - TauD has also been observed i.e. 24.6 kcal/mol [37]. Comparable values were also obtained for non-heme iron halogenases (also members of the ODD family), HctB [38] or SyrB2 [39]. The resulting intermediate t-Int has an energy of 8.8 kcal/mol (Fig. 5). There are slight changes in the geometry of the QM part i.e. distances between the Fe ion and SIN, axial His-295 and the oxo ligand increased from 2.00, 2.09, 1.61 to 2.12, 2.24, 1.90 Å, respectively, compared to the enzyme-substrate complex t-*E*-S (Fig. 6A & C). There is also a slight increase in distance between the equatorial His238 and Fe; from 2.09 to 2.18 Å. Next, we calculated the free energy barrier (t-TS2) for the OH rebound step, which is 8.4 kcal/mol (Fig. 5) and the distance between OH and the radical carbon atom is 2.25 Å (Fig. 6D). The final hemiacetal (Fig. 6E) product formed after OH rebound has an energy of −20.8 kcal/mol.

*3.4.1.2. T6ODM:SIN:oripavine.* For the oripavine complex, the calculated energy barrier (o-TS1) for hydrogen abstraction by the ferryl (Fe(IV)-oxo) intermediate is 22.3 kcal/mol (Fig. 5) and the distance between the oxo ligand and hydrogen to be abstracted is 1.23 Å (Fig. 7B). The high energy barrier for hydrogen abstraction is consistent with the

**Table 2**
Fe spin population for stationary points along the reaction coordinate.

| | T6ODM:SIN:thebaine | T6ODM:SIN:oripavine |
|---|---|---|
| *E*-S-Fe(IV) | 3.209 | 3.156 |
| TS1-Fe(III) | 4.129 | 4.189 |
| Int-Fe(III) | 4.244 | 4.231 |
| TS2-Fe(III) | 4.043 | 4.090 |
| E-P-Fe(II) | 3.767 | 3.801 |

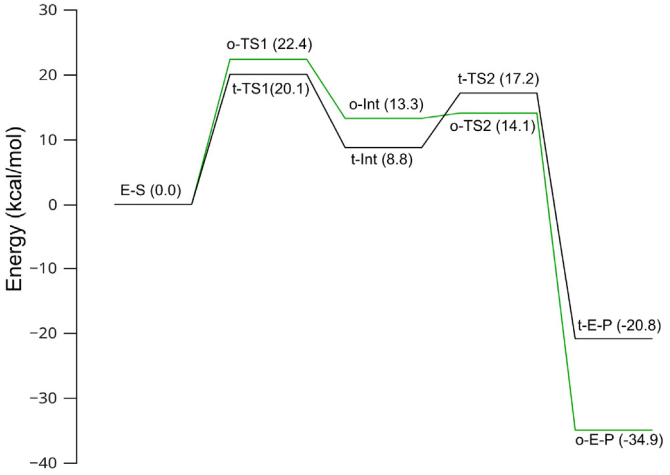


**Fig. 5.** Energy profile for T6ODM-catalysed hydroxylation of C6-bound methoxyl groups in the course of demethylation reactions of thebaine (black) and oripavine (green).

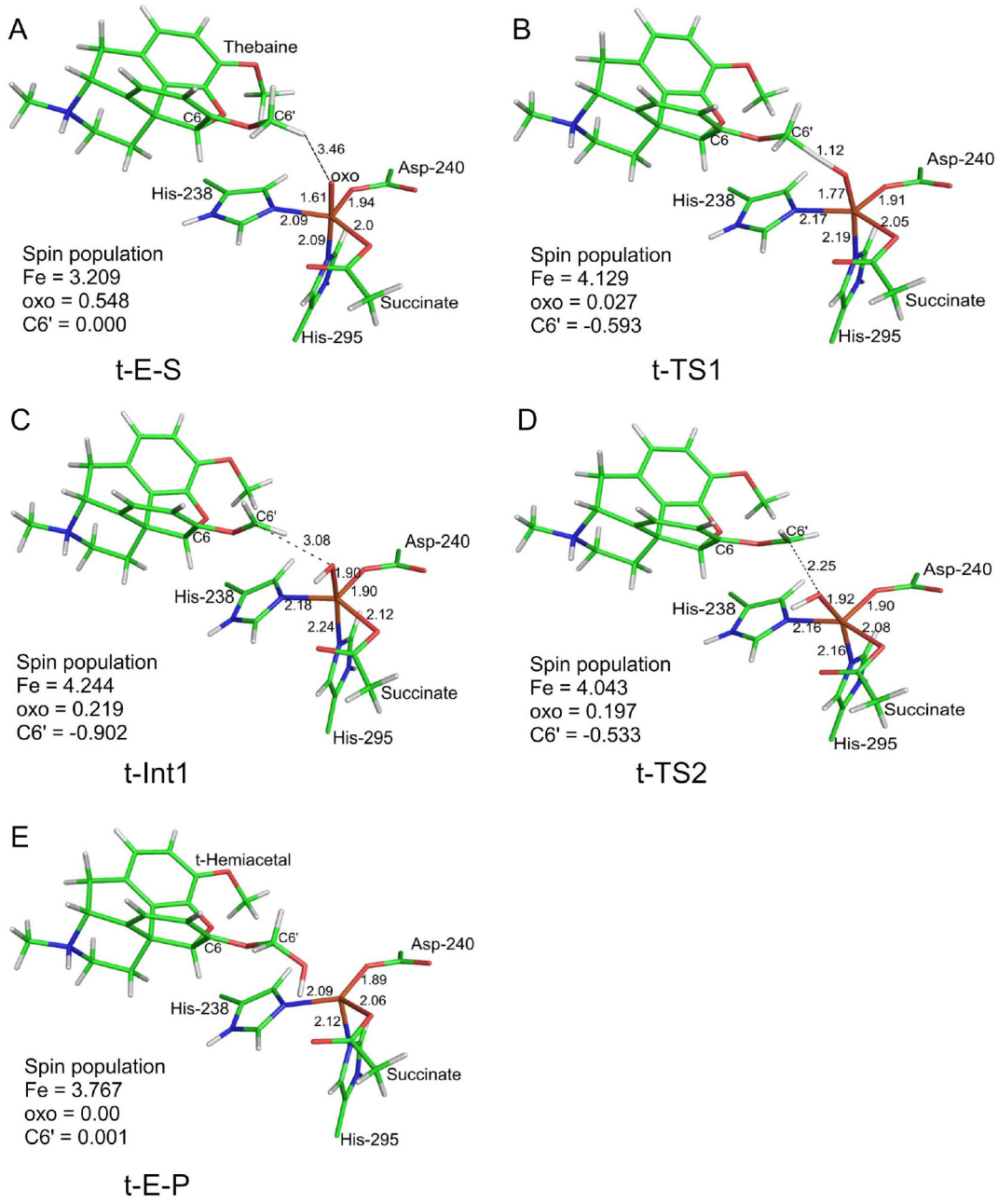


**Fig. 6.** Structures of the QM-part of the QM/MM model for stationary points along the reaction coordinate for demethylation of thebaine.

result obtained for thebaine. The intermediate (o-Int) formed after hydrogen abstraction has an energy of 13.3 kcal/mol (Fig. 5). Similar to thebaine-derived intermediate, t-Int, o-Int has slight changes in distances between Fe and its ligands. There is an increase in distances between Fe and succinate, axial His-295 and oxo from 1.91, 2.09, 1.63 to 2.11, 2.25, 1.92 Å, respectively. Equatorial His238 - Fe distance also increases slightly, from 2.12 to 2.18 Å (Fig. 7A & C). Next, we calculated the energy barrier (o-TS2) of OH rebound to the C6-O-$CH_2$ radical, which is 0.8 kcal/mol (Fig. 5), and the distance between OH and the carbon atom in the transition state o-TS2 is 1.23 Å (Fig. 7D). The hemiacetal (Fig. 7E) product formed after the OH-rebound step has an energy of −34.9 kcal/mol (Fig. 5).

*3.4.2. Formation of the final products from hemiacetals*

In the above described steps of the enzymatic reactions, thebaine and oripavine are both transformed into hemiacetals which will further deformylate and tautomerize to form neopinone and neomorphinone, respectively. Here we have used DFT and cluster models to calculate energy barriers for these two reactions. In the first step, hemiacetal decomposes into an enolic form of the final product and formaldehyde (Figs. 8A & 9A), and in the next step reverse keto-enol tautomerization results in the formation of neopinone and neomorphinone (Figs. 8B & 9B), respectively.

The calculated energy barrier (t-H-TS3) for deformylation of t-hemiacetal to t-enol is 20.06 kcal/mol, and the similar energy barrier (o-H-TS3) was calculated for deformylation of o-hemiacetal i.e. 20.01 kcal/mol (Fig. 10A). Deformylation of both hemiacetals to enols is mediated by a molecule of water. These calculated energy barriers are quite high but not unprecedented. It has been reported that the energy barrier for the decomposition of methanethiol decreased by 15 kcal/mol when the process was mediated by one molecule of water, and by 27 kcal/mol when two molecules of water were present

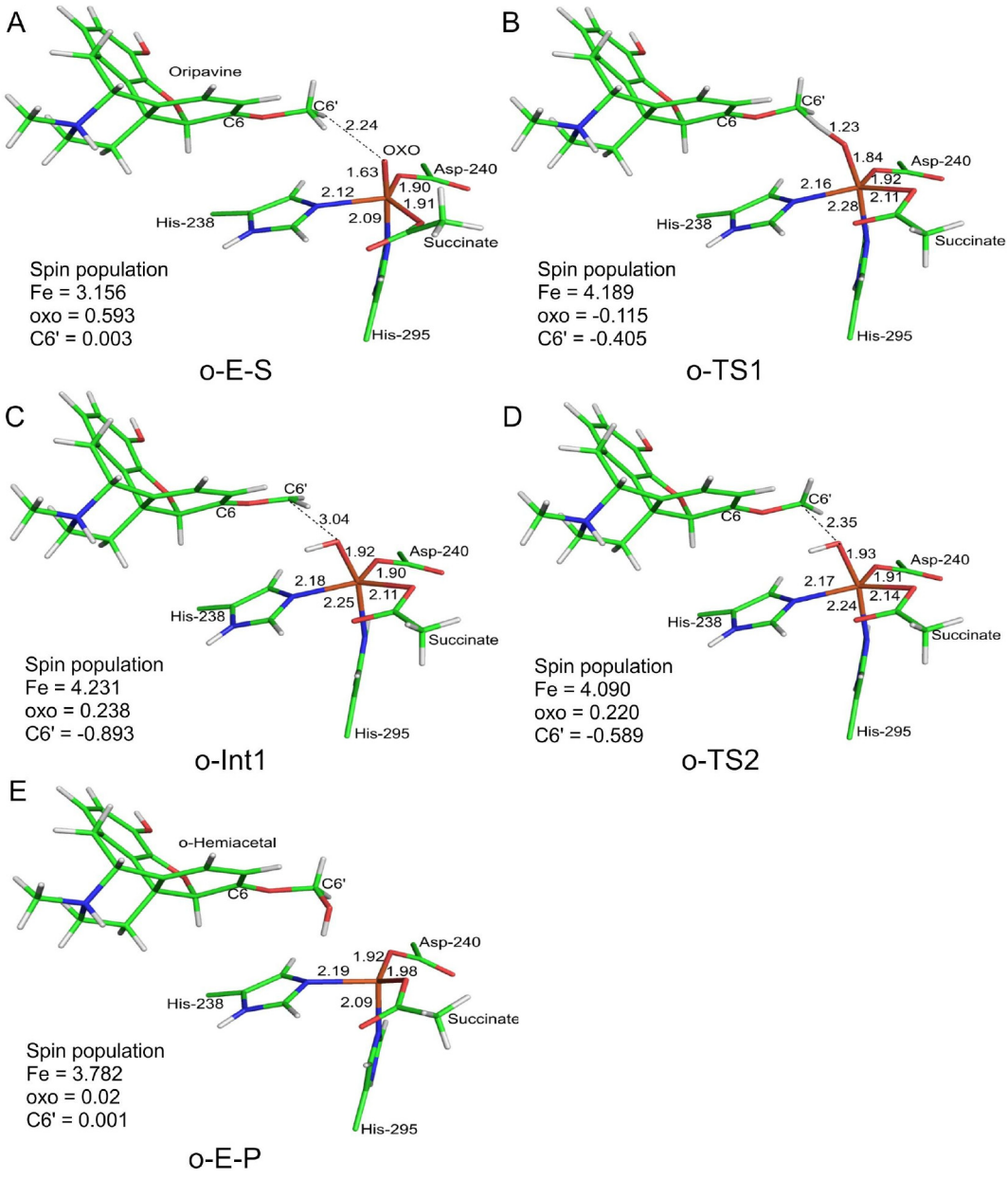


**Fig. 7.** Structures of the QM-part of the QM/MM model for stationary points along the reaction coordinate for demethylation of oripavine.

[40]. ONIOM calculations for the same decomposition reaction gave an energy barrier of 21.3 kcal/mol when two water molecules were included in the QM region and decreased further to 18.3 kcal/mol by increasing the number of water molecules in the QM region up to eight [41]. Thus, in light of these published results, our calculated energy barriers seem very reasonable. Further, we calculated the energy barriers for the formation of neopinone and neomorphinone from their respective enols by enol-keto tautomerization; for neopinone it was calculated to be 12.4 kcal/mol (t-*E*-TS4) and for neomorphinone 10.0 kcal/mol (o-E-TS4) (Fig. 10B). These tautomerization reactions are mediated by two water molecules carrying the proton from the OH group to the C7 atom. Finally, it is worth noting that before calculating the energy barriers for the two steps reaction of neopinone formation i.e. deformylation and tautomerization, we also tried direct $H^+$ transfer from OH of t-Hemiacetal to C-atom in the ring, so that neopinone would form directly from t-Hemiacetal upon release of formaldehyde. However, the calculated energy barrier for this direct reaction is very high, i.e. 31.9 kcal/mol. Thus, we considered the two steps reaction for formation of the final product neopinone from hemiacetal, which turned out to be far more plausible.

## 4. Conclusions

Despite many various attempts undertaken so far we have not been able to obtain crystal structures of the T6ODM:NOG:thebaine complex, hence, we decided to resort to other methods capable of providing insights into its structure. Extended molecular docking and molecular dynamics simulations for 1:1 and 1:2 T6ODM:substrate complexes revealed that: 1) in 1:1 complexes the substrate molecule binds at the distal binding site, which is located too far from the metal cofactor to support catalysis, and 2) 1:2 complexes are stable and the substrate molecule bound in the immediate proximity to the metal cofactor presents the right (C6-bound) methoxy group towards the iron ion. Results obtained with the Multi-Parametric Surface Plasmon Resonance method strongly support the 1:2 stoichiometry of the T6ODM:thebaine complex. Key residues responsible for binding the substrate molecule in

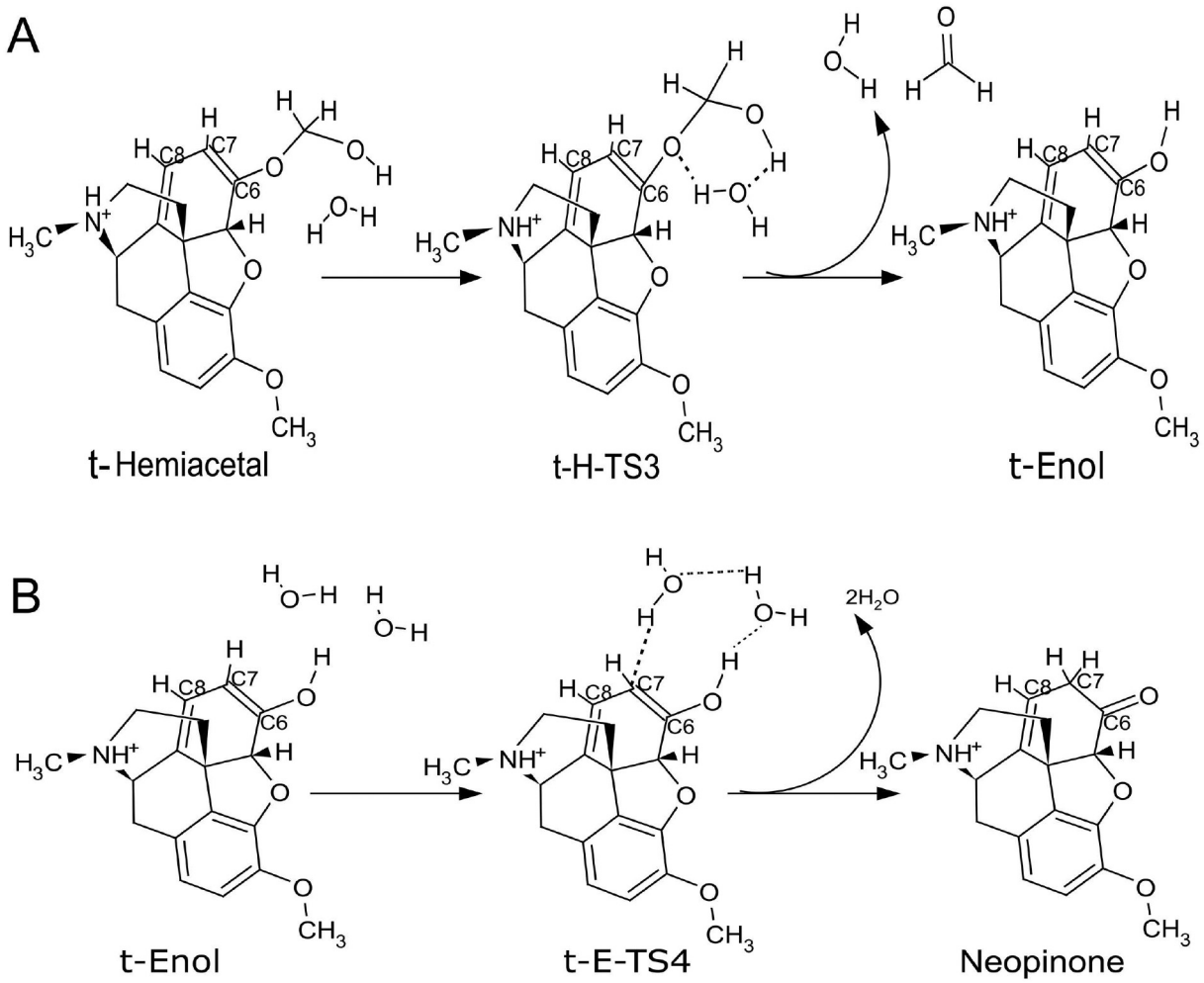


**Fig. 8.** Reaction scheme for formation of neopinone from t-hemiacetal. A) First step - transformation of t-hemiacetal to t-enol (deformylation reaction), B) Second step - t-enol to neopinone tautomerization.

the distal site are: Val-128, Glu-133, Met-150 and Arg-219, whereas the substrate molecule proximal to the metal interacts with the other substrate molecule and Asp-144, Leu-235 and Leu-353. Obtained macromolecular models for the enzyme-substrate complexes were used as starting points for QM/MM investigations on the enzymatic reaction mechanism of T6ODM. The computed reaction energy profiles revealed that the hydrogen atom abstraction step is characterized by a larger barrier than the subsequent OH-rebound, which is typical for iron-dependent hydroxylases [38,42]. The barrier for the hydrogen atom abstraction is relatively high, therefore it is tempting to speculate that the enzyme compromises stabilisation of the transition state to facilitate the regioselectivity of the reaction or the ability to accept two different substrates. We believe that the provided here atomic-level insights into structures and energetics of key stationary points along the T6ODM catalytic reaction coordinate will spawn further studies on *O*-demethylases, in particular T6ODM and a closely related CODM.

## CRediT authorship contribution statement

**Sangita Kachhap:**Methodology, Investigation, Data curation, Writing - original draft, Writing - review & editing, Visualization.**Zuzanna Wojdyla:**Methodology, Investigation, Data curation, Writing - original draft, Writing - review & editing, Visualization.**Paulina Komorek:**Methodology, Investigation, Data curation, Writing - original draft, Writing - review & editing, Visualization.**Anna Kluza:**Methodology, Resources, Investigation, Writing - original draft, Writing - review & editing. **Katarzyna Kurpiewska:**Methodology, Resources, Investigation, Writing - original draft, Writing - review & editing.**Barbara Jachimska:** Methodology, Resources, Writing - original draft, Writing - review & editing.**Tomasz Borowski:**Conceptualization, Validation, Writing - original draft, Writing - review & editing, Visualization, Supervision, Project administration, Funding acquisition.

## Declaration of competing interest

Authors declare no conflict of interest.

## Acknowledgements

This research project was supported by grant No UMO-2014/14/E/NZ1/00053 from the National Science Centre, Poland. This research was supported in part by PL-Grid Infrastructure. Computations were performed at Academic Computer Centre Cyfronet AGH.

## Appendix A. Supplementary data

Fig. S1 presenting a timeline of MD simulations, Fig. S2 presenting docking results.

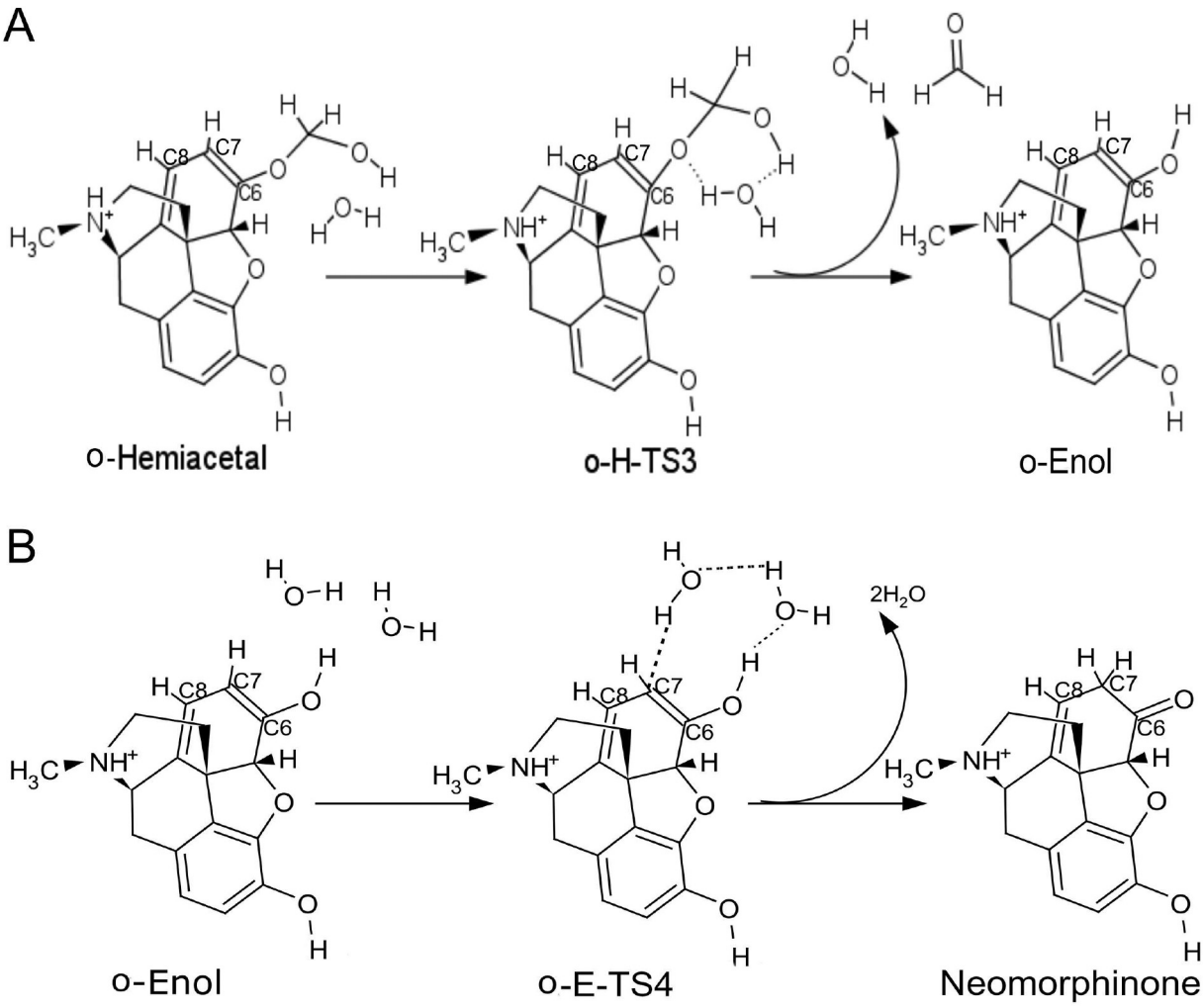


**Fig. 9.** Formation of neomorphinone from o-hemiacetal. A) o-hemiacetal to o-enol transformation (deformylation reaction), B) o-enol to neomorphinone tautomerization.

Gaussian 16 input and output files for all optimized structures have been deposited at the Mendeley Data repository, and they are freely available at: doi: 10.17632/vfmv2pcfj9.2. Optimised structures have been deposited in the ioChem database and are freely available at: https://doi.org/10.19061/iochem-bd-4-21. Supplementary data to this article can be found online at doi:https://doi.org/10.1016/j.ijbiomac.2020.07.030.

## References

[1] C.Q. Herr, R.P. Hausinger, Amazing diversity in biochemical roles of Fe(II)/2-Oxoglutarate oxygenases, Trends Biochem. Sci. 43 (2018) 517–532.
[2] S.C. Farrow, P.J. Facchini, Dioxygenases catalyzeo-demethylation and O,O-demethylenation with widespread roles in benzylisoquinoline alkaloid metabolism in opium poppy, J. Biol. Chem. 288 (2013) 28997–29012.
[3] A. Singh, I.M. Menéndez-Perdomo, P.J. Facchini, Benzylisoquinoline alkaloid biosynthesis in opium poppy: an update, Phytochem. Rev. 240 (2019) 19–32.
[4] A. Kluza, E. Niedzialkowska, K. Kurpiewska, Z. Wojdyla, M. Quesne, E. Kot, P.J. Porebski, T. Borowski, Crystal structure of thebaine 6-O-demethylase from the morphine biosynthesis pathway, J. Struct. Biol. 202 (2018) 229–235.
[5] R.C. Wilmouth, J.J. Turnbull, R.W.D. Welford, I.J. Clifton, A.G. Prescott, C.J. Schofield, Structure and mechanism of anthocyanidin synthase from Arabidopsis thaliana, Structure 10 (2002) 93–103.
[6] R.W.D. Welford, I.J. Clifton, J.J. Turnbull, S.C. Wilson, C.J. Schofield, Structural and mechanistic studies on anthocyanidin synthase catalysed oxidation of flavanone substrates: the effect of C-2 stereochemistry on product selectivity and mechanism, Org. Biomol. Chem. 3 (2005) 3117–3126.
[7] C.H. Mahler, E.D. Stevens, M.L. Trudell, S.P. Nolan, (−)-Thebaine, Acta Crystallogr. Sect. C Cryst. Struct. Commun. 52 (1996) 3193–3195.
[8] D.R. Lide, ed., Handbook of Chemistry and Physics, 76th ed., CRC Press, n.d.
[9] A.D. Becke, Density-functional thermochemistry. III. The role of exact exchange, J. Chem. Phys. 98 (1993) 5648–5652.
[10] S. Grimme, S. Ehrlich, L. Goerigk, Effect of the damping function in dispersion corrected density functional theory, J. Comput. Chem. 32 (2011) 1456–1465.
[11] J. Wang, R.M. Wolf, J.W. Caldwell, P.A. Kollman, D.A. Case, Development and testing of a general amber force field, J. Comput. Chem. 25 (2004) 1157–1174.
[12] J. Wang, P. Cieplak, P.A. Kollman, How well does a restrained electrostatic potential (RESP) model perform in calculating conformational energies of organic and biological molecules? J. Comput. Chem. 21 (2000) 1049.
[13] X.W. and P.A.K. D.A. Case, V. Babin, J.T. Berryman, R.M. Betz, Q. Cai, D.S. Cerutti, T.E. Cheatham, T.A. Darden III, R.E. Duke, H. Gohlke, A.W. Goetz, S. Gusarov, N. Homeyer, P. Janowski, J. Kaus, I. Kolossváry, A. Kovalenko, T.S. Lee, S. LeGrand, T. Luchko, R. Luo B., AMBER 14, Univ. California, San Fr, 2014.
[14] W.L. Jorgensen, J. Chandrasekhar, J.D. Madura, R.W. Impey, M.L. Klein, Comparison of simple potential functions for simulating liquid water, J. Chem. Phys. 79 (1983) 926–935.
[15] Y. Duan, C. Wu, S. Chowdhury, M.C. Lee, G. Xiong, W. Zhang, R. Yang, P. Cieplak, R. Luo, T. Lee, J. Caldwell, J. Wang, P. Kollman, A point-charge force field for molecular mechanics simulations of proteins based on condensed-phase quantum mechanical calculations, J. Comput. Chem. 24 (2003) 1999–2012.
[16] J.M. Seminario, Calculation of intramolecular force fields from second-derivative tensors, Int. J. Quantum Chem. 60 (1996) 1271–1277.
[17] M.J. Frisch, G.W. Trucks, H.B. Schlegel, G.E. Scuseria, M.A. Robb, J.R. Cheeseman, G. Scalmani, V. Barone, G.A. Petersson, H. Nakatsuji, X. Li, M. Caricato, A. Marenich, J. Bloino, B.G. Janesko, R. Gomperts, B. Mennucci, H.P. Hratchian, J.V. Ortiz, A.F. Izmaylov, J.L. Sonnenberg, D. Williams-Young, F. Ding, F. Lipparini, F. Egidi, J. Goings, B. Peng, A. Petrone, T. Henderson, D. Ranasinghe, V.G. Zakrzewski, J. Gao, N. Rega, G. Zheng, W. Liang, M. Hada, M. Ehara, K. Toyota, R. Fukuda, J. Hasegawa, M. Ishida, T. Nakajima, Y. Honda, O. Kitao, H. Nakai, T. Vreven, K. Throssell, J.A. Montgomery Jr., J.E. Peralta, F. Ogliaro, M. Bearpark, J.J. Heyd, E. Brothers, K.N. Kudin, V.N. Staroverov, T. Keith, R. Kobayashi, J. Normand, K. Raghavachari, A. Rendell, J.C. Burant, S.S. Iyengar, J. Tomasi, M. Cossi, J.M. Millam, M. Klene, C. Adamo, R. Cammi, J.W. Ochterski, R.L. Martin, K. Morokuma, O. Farkas, J.B. Foresman, D.J. Fox, Gaussian 09, Revision D.01, Gaussian, Inc, Wallingford CT, 2013.

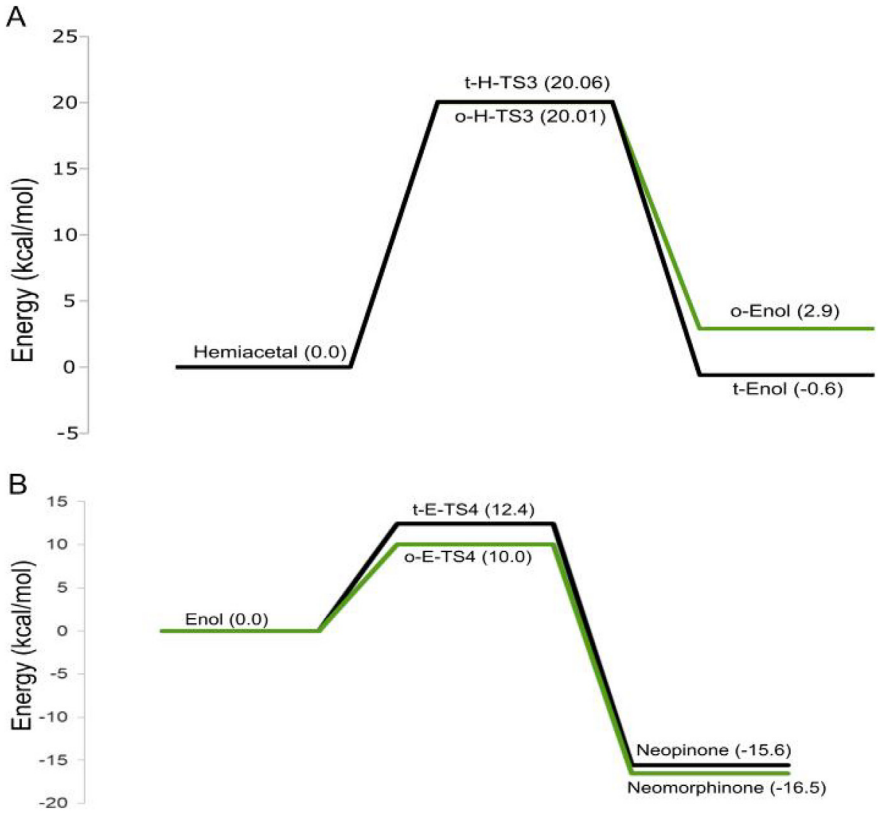


**Fig. 10.** Energy profile for transformation of hemiacetals to ketones. A) formation of enols via deformylation and B) reverse keto-enol tautomerization yielding neopinone and neomorphinone.


[18] G.M. Morris, R. Huey, W. Lindstrom, M.F. Sanner, R.K. Belew, D.S. Goodsell, A.J. Olson, AutoDock4 and AutoDockTools4: automated docking with selective receptor flexibility, J. Comput. Chem. 30 (2009) 2785–2791.

[19] J.P. Ryckaert, G. Ciccotti, H.J. Berendsen, Numerical integration of the cartesian equations of motion of a system with constraints: molecular dynamics of n-alkanes, J. Comput. Phys. 23 (1977) 327–341.

[20] S. Miyamoto, P.A. Kollman, Settle: an analytical version of the SHAKE and RATTLE algorithm for rigid water models, J. Comput. Chem. 13 (1992) 952–962.

[21] T. Darden, D. York, L. Pedersen, Particle mesh Ewald: an N ·log(N) method for Ewald sums in large systems, J. Chem. Phys. 98 (1993) 10089–10092.

[22] D.R. Roe, T.E. Cheatham, PTRAJ and CPPTRAJ: software for processing and analysis of molecular dynamics trajectory data, J. Chem. Theory Comput. 9 (2013) 3084–3095.

[23] M.J. Frisch, G.W. Trucks, H.B. Schlegel, G.E. Scuseria, M.A. Robb, J.R. Cheeseman, G. Scalmani, V. Barone, G.A. Petersson, H. Nakatsuji, X. Li, M. Caricato, A.V. Marenich, J. Bloino, B.G. Janesko, R. Gomperts, B. Mennucci, H.P. Hratchian, J.V. Ortiz, A.F. Izmaylov, J.L. Sonnenberg, D. Williams-Young, F. Ding, F. Lipparini, F. Egidi, J. Goings, B. Peng, A. Petrone, T. Henderson, D. Ranasinghe, V.G. Zakrzewski, J. Gao, N. Rega, G. Zheng, W. Liang, M. Hada, M. Ehara, K. Toyota, R. Fukuda, J. Hasegawa, M. Ishida, T. Nakajima, Y. Honda, O. Kitao, H. Nakai, T. Vreven, K. Throssell, J.A. Montgomery Jr., J.E. Peralta, F. Ogliaro, M.J. Bearpark, J.J. Heyd, E.N. Brothers, K.N. Kudin, V.N. Staroverov, T.A. Keith, R. Kobayashi, J. Normand, K. Raghavachari, A.P. Rendell, J.C. Burant, S.S. Iyengar, J. Tomasi, M. Cossi, J.M. Millam, M. Klene, C. Adamo, R. Cammi, J.W. Ochterski, R.L. Martin, K. Morokuma, O. Farkas, J.B. Foresman, D.J. Fox, Gaussian 16, Gaussian (2016).

[24] L.W. Chung, W.M.C. Sameera, R. Ramozzi, A.J. Page, M. Hatanaka, G.P. Petrova, T.V. Harris, X. Li, Z. Ke, F. Liu, H.-B. Li, L. Ding, K. Morokuma, The ONIOM method and its applications, Chem. Rev. 115 (2015) 5678–5796.

[25] F. Weigend, R. Ahlrichs, Balanced basis sets of split valence, triple zeta valence and quadruple zeta valence quality for H to Rn: design and assessment of accuracy, Phys. Chem. Chem. Phys. 7 (2005) 3297.

[26] M. Cossi, N. Rega, G. Scalmani, V. Barone, Energies, structures, and electronic properties of molecules in solution with the C-PCM solvation model, J. Comput. Chem. 24 (2003) 669–681.

[27] R. Bakhtiar, Surface plasmon resonance spectroscopy: a versatile technique in a biochemist's toolbox, J. Chem. Educ. 90 (2013) 203–209.

[28] M. Citartan, S.C.B. Gopinath, J. Tominaga, T.-H. Tang, Label-free methods of reporting biomolecular interactions by optical biosensors, Analyst 138 (2013) 3576.

[29] K.L.M. Moran, D. Lemass, R. O'Kennedy, Surface plasmon resonance–based immunoassays, Handb. Immunoass. Technol, Elsevier 2018, pp. 129–156.

[30] B. Jachimska, K. Tokarczyk, Combining surface plasmon resonance and quartz crystal microbalance to determine hydration of dendrimer monolayers, J. Phys. Chem. C 120 (2016) 19678–19685.

[31] A. Manglik, A.C. Kruse, T.S. Kobilka, F.S. Thian, J.M. Mathiesen, R.K. Sunahara, L. Pardo, W.I. Weis, B.K. Kobilka, S. Granier, Crystal structure of the μ-opioid receptor bound to a morphinan antagonist, Nature 485 (2012) 321–326.

[32] J. Olah, A.J. Mulholland, J.N. Harvey, Understanding the determinants of selectivity in drug metabolism through modeling of dextromethorphan oxidation by cytochrome P450, Proc. Natl. Acad. Sci. 108 (2011) 6050–6055.

[33] M.J.I. Paine, L.A. McLaughlin, J.U. Flanagan, C.A. Kemp, M.J. Sutcliffe, G.C.K. Roberts, C.R. Wolf, Residues glutamate 216 and aspartate 301 are key determinants of substrate specificity and product regioselectivity in cytochrome P450 2D6, J. Biol. Chem. 278 (2003) 4021–4027.

[34] P. Komorek, M. Wałek, B. Jachimska, Mechanism of lysozyme adsorption onto gold surface determined by quartz crystal microbalance and surface plasmon resonance, Bioelectrochemistry 135 (2020), 107582. .

[36] A. Wójcik, M. Radoń, T. Borowski, Mechanism of $O_2$ activation by α-Ketoglutarate dependent oxygenases revisited. A quantum chemical study, J. Phys. Chem. A 120 (2016) 1261–1274.

[37] S. Ye, F. Neese, Nonheme oxo-iron(IV) intermediates form an oxyl radical upon approaching the C-H bond activation transition state, Proc. Natl. Acad. Sci. 108 (2011) 1228–1233.

[38] A. Timmins, S.P. de Visser, A comparative review on the catalytic mechanism of non-heme Iron hydroxylases and halogenases, Catalysts 8 (2018) 314.

[39] T. Borowski, H. Noack, M. Radoń, K. Zych, P.E.M. Siegbahn, Mechanism of selective halogenation by SyrB2: a computational study, J. Am. Chem. Soc. 132 (2010) 12887–12898.

[40] S. Inaba, Theoretical study of decomposition of methanediol in aqueous solution, J. Phys. Chem. A 119 (2015) 5816–5825.

[41] S. Inaba, W.M.C. Sameera, Dehydration of methanediol in aqueous solution: an ONIOM(QM/MM) study, J. Phys. Chem. A 120 (2016) 6670–6676.

[42] M.G. Quesne, T. Borowski, S.P. de Visser, Quantum mechanics/molecular mechanics modeling of enzymatic processes: caveats and breakthroughs, Chem. - A Eur. J. 22 (2016) 2562–2581.

[43] ChemAxon, MarvinSketch 18.20, 2018.